Evolution of in-plane heat transport in tellurium from 2D to 3D

Yanhua Cheng [a], Jinlong Ma [a], Yaxin Xu [a], Guoqing Sun [a], Xiulin Ruan [b],**, Xiaobing Luo [a],*

[a] *School of Energy and Power Engineering, Huazhong University of Science and Technology, Wuhan, 430074, PR China*
[b] *School of Mechanical Engineering and the Birck Nanotechnology Center, Purdue University, West Lafayette, IN, 47907-2088, USA*

ARTICLE INFO

ABSTRACT

Tellurene (Te) has attracted tremendous interest due to its outstanding electronic, thermoelectric, and opto-electronic properties. Recently, it is found that 2-layer Te exhibits an abnormal anisotropy of in-plane thermal conductivity. This inspires the current investigation, where the thickness dependence of in-plane thermal conductivities of tellurium from 2D to 3D is obtained by first-principles calculations and Monte Carlo simulations. Two intriguing phenomena are discovered: (1) Thermal conductivity rebound (TCR), *i.e.*, the thermal conductivity first reduces and then increases with the increasing thickness. The predicted lowest point emerges between 6-layer to 15-layer; (2) Thermal anisotropy reversal (TAR), *i.e.*, the in-plane thermal conductivity anisotropy reverses from abnormal ($\kappa_\perp/\kappa_\parallel > 1$) to normal ($\kappa_\perp/\kappa_\parallel < 1$) with increasing thickness. The predicted reversal point occurs at around 7-layer. To understand these phenomena, the frequency- and mode-dependent analyses on phonon group velocity and relaxation time are performed. As the thickness increases, the relaxation time almost monotonically increases, whereas the velocity of low-frequency optical (LFO) phonons shows the same varying trend with thermal conductivity, making it the main factor accounting for the TCR and TAR. The trend of the group velocity of LFO phonons can be attributed to the lattice expansion, which diminishes the covalent-like quasi-bonding (CLQB) in the cross-chain direction. The layer-dependent thermal transport of Te revealed in this work is expected to provide guidance for Te-based functional devices, for instance, the thermoelectric system where the lowest thermal conductivity is favorable.

1. Introduction

Two-dimensional (2D) materials have stimulated a rapid development of micro-/nano-scale electronic, optoelectronic, thermoelectric, and other energy conversion devices since the successful fabrication of graphene [1–8]. Thermal transport in 2D materials is one of the most important topics due to the critical role it plays in the performance and thermal management of these devices. Dimension decrease brings enormous changes of the in-plane thermal transport to 2D materials, compared to their three-dimensional (3D) counterparts. For instance, the in-plane thermal conductivity of suspended graphene at room temperature is reported to be larger than that of graphite. High-quality monolayer hexagonal boron nitride (h-BN) was measured to have an in-plane thermal conductivity of ~751 W/mK [9] at room temperature, higher than that of its bulk counterpart, ~408 W/mK [10,11]. Molybdenum disulfide (MoS_2) also shows larger in-plane room-temperature (RT) thermal conductivities in its monolayer (34.5 W/mK) than in bulk (18.6 W/mK) [12–14]. Interestingly, the trend is reversed in black

phosphorus (BP), whose monolayer has a lower in-plane RT thermal conductivity than the bulk value [15,16]. It can be naturally anticipated that the significant difference of thermal transport between the 2D and 3D allotropes cannot occur in a sudden. Rather, the evolution, as reflected by the thickness-dependent thermal transport in these 2D materials, is of high interest.

In the past decade, thickness-dependent heat transport of 2D materials has been extensively investigated. In terms of the in-plane thermal conductivity, three types of thickness dependence were found [17]. In the first type, as reported in graphene and h-BN, the in-plane thermal conductivities decrease with increasing number of layers and converges to bulk at around 5- and 4-layer, respectively [9,18,19]. In the second type, which is opposite to the first, the in-plane thermal conductivity increases with thickness represented by BP [15,16,20,21]. In the third type, a non-monotonical dependence on the thickness was recently found in several transition-metal dichalcogenides (TMDs) and trichalcogenides (TMTs), including MoS_2, WTe_2, and TiS_3. Specifically, the in-plane thermal conductivity decreases first and then increases with thickness [22–24]. Another aspect of the thermal transport is the

Abbreviations

2D	two-dimensional
3D	three-dimensional
AC	along-chain
AR	anisotropy ratio
BP	black phosphorus
CB(s)	covalent bond(s)
CC	cross-chain
CLQB(s)	covalent-like quasi-bonding(s)
DFT	density function theory
DFT-TS	density function theory-Tkatchenko-Scheffler
GGA	generalized gradient approximation
h-BN	hexagonal boron nitride
ICOHP(s)	integrated crystal orbital Hamilton population(s)
LFO	low-frequency optical
MC	Monte Carlo
MD	molecular dynamics
MFP	mean free path
PAW	projector augmented-wave
PBE	Perdew-Burke-Ernzerhof
PBTE	Peierls Boltzmann transport equation
PDOS	phonon density of states
RT	room-temperature
TAR	thermal anisotropy reversal
TCR	thermal conductivity rebound
TDEP	temperature-dependent effective potential
TMD(s)	transition-metal dichalcogenide(s)
TMT(s)	transition-metal trichalcogenides(s)
vdW	van der Waals

thermal anisotropy. Graphene, BP, WTe₂, and tellurium (>15 nm) have nearly constant in-plane anisotropy ratios (ranging from ∼0.4 to ∼0.7) for different thickness [15,21,25,26]. Additionally, they show a normal thermal anisotropy, i.e., their out-of-plane thermal conductivity (where atomic interaction is van der Waals force) is smaller than the in-plane thermal conductivity (where the atomic bonding is covalent). However, in our prior work [27], an abnormal in-plane thermal conductivity anisotropy was identified in bilayer tellurene, where the cross-chain thermal conductivity is larger than the along-chain thermal conductivity. Apparently, the thickness-dependent thermal transport varies in different 2D materials, and it needs to be explored.

Some studies have been implemented to explore the physics underlying the different thickness-dependent heat transport in 2D materials. Qiu et al. [28] attributed the non-monotonic thickness-dependent thermal conductivity of few-quintuple Bi₂Te₃ to the interplay of Umklapp scattering and boundary scattering. Gu et al. [23] and Wu et al. [22] found the change of phonon dispersion and the thickness-induced anharmonicity are highly related to the reduced thermal conductivity of MoS₂ from monolayer to 4-layer and the non-monotonic thickness-dependent in-plane thermal conductivity in Td-WTe₂. Fu et al. [29] proposed the concept of phonon confinement to interpret the different thermal behaviors when the thickness is smaller or larger than the phonon confinement size in argon and silicon thin films, which was subsequently referred by Liu et al. [24] to explain the non-monotonic in-plane thermal conductivity and anisotropy in TiS₃. However, a unified theory is still lacking to provide universal understanding for the various thickness-dependent phenomena in 2D materials.

Recently, tellurene, a new 2D material, has attracted tremendous research interest owing to its outstanding electronic, thermoelectric, piezoelectric, and optoelectronic properties [30–41]. Thermal transport in monolayer, bilayer, many-layer (>15 nm), and bulk tellurium (Te) have been investigated in prior works [25,27,42–47]. Nevertheless, to the best of our knowledge, the thermal transport of very thin (<10 nm) Te films has not been reported yet, neither through experimental nor theoretical studies, leaving an incomplete picture of the thickness dependent heat transport of Te through 2D to 3D. Moreover, we recently found the abnormal in-plane thermal conductivity anisotropy in bilayer tellurene, opposite to the normal anisotropy in bulk Te and other 2D materials [27]. This leaves a puzzle: how does the in-plane thermal anisotropy of Te evolve from 2D to 3D? Thereby, a full understanding of thickness-dependent heat transport in Te is required.

Herein, we study the in-plane thermal transport in 2- to 5-layer tellurene and bulk Te using first principle Peierls Boltzmann transport equation (PBTE) method, and the films with thickness ranging from 10 to 5000 nm using phonon Monte Carlo simulation. A complete evolution picture of the in-plane thermal transport from 2D to 3D Te is presented, and two features are discovered: (1) Non-monotonic thickness-

dependence of the in-plane thermal conductivity. Both the cross-chain (CC) thermal conductivity $\kappa_\perp$ and the along-chain (AC) thermal conductivity $\kappa_\parallel$ first decrease and then rise with the number of layers. We name this feature as thermal conductivity rebound (TCR). The predicted lowest $\kappa_\perp$ and $\kappa_\parallel$ appears between ∼ 6-layer to ∼15-layer. (2) In-plane thermal anisotropy of Te gradually changes from abnormal ($\kappa_\perp/\kappa_\parallel > 1$) to normal ($\kappa_\perp/\kappa_\parallel < 1$) with increasing thickness, which is identified as thermal anisotropy reversal (TAR). The predicted reversal point occurs at around 7-layer. To explore the physics behind these two interesting phenomena, phonon properties, phonon dispersions, lattice constants are calculated and analyzed. According to our analyses, TCR results from the joint effect of the non-monotonically changing group velocity of the low-frequency optical (LFO) phonons (0.5–2.0 THz), increasing phonon relaxation time, and weakening thickness effect; TAR is mainly caused by the fast-decreasing CC group velocity ($v_\perp$) and slowly-changing AC group velocity ($v_\parallel$) of the LFO phonons. The crystal orbital Hamilton population analysis is further integrated to show that the variation of the LFO phonon properties can be attributed to the lattice expansion and subsequent CLQB diminishing. This work may provide fundamental insight to thermal transport in Te-based electronic devices and thermoelectric materials, and could broaden the general understanding of the thermal transport physics in 2D materials.

2. Methodology and computational details

In previous studies, investigation on thickness dependent thermal transport of layered materials is usually implemented by first-principles calculation, molecular dynamics (MD) simulations, or lattice dynamics (LD) combined BTE calculations [23,24,28,29,48,49]. First-principles calculation has high accuracy in thermal conductivity prediction since it needs no empirical parameters, while the thickness that it is able to explore is limited by the computational cost [24]. MD can include all high order anharmonicity, but the film thickness that can be explored is also limited by the computational costs, which scales linearly with the number of atoms in the simulation cell [23,28,29]. In addition, the applicability of MD is weak for new materials like tellurene due to the lack of appropriate empirical interatomic potentials. LD combined BTE method requires phonon transport properties as input, so its accuracy depends on the accuracy of the input. However, for efficiency, the phonon transport properties of bulk are generally utilized for different film thickness, with some approximations such as Fuchs-Sondheimer boundary scattering and phonon depletion employed to compensate for the discrepancy between the phonon transports of films and bulk [29,48,49]. LD method thus can reasonably predict the thermal conductivity of thick films while it fails to estimate the thermal conductivity of very thin film. Neither first-principles calculation, MD, or LD method can individually investigate the full thermal transport picture of Te from 2D

to 3D (from several angstroms to thousands of nanometers). Herein, first-principles calculation is used for the prediction of very thin Te films and bulk Te while MC BTE simulation is employed for the prediction of thick Te films (10–5000 nm), presenting a full picture from 2D to 3D.

2.1. First principle PBTE method

In the framework of first principle PBTE method, thermal conductivity is given by:

$$\kappa_{\alpha\beta} = \frac{1}{k_B T^2} \frac{1}{8\pi^3} \sum_\lambda \int_{BZ} f_0\left(\omega_{\lambda,q}\right) \left[f_0\left(\omega_{\lambda,q}\right) + 1\right] \hbar^2 \omega_{\lambda,q}^2 v_{\lambda,q}^\alpha v_{\lambda,q}^\beta \tau_{\lambda,q} dq, \tag{1}$$

where ω, v, and τ represent phonon frequency, group velocity, and relaxation time, respectively. f_0 is phonon distribution function. T stands for temperature. k_B and $\hbar$ are Boltzmann constant and reduced Plank constant. Subscripts α and β denote directions. BZ is the abbreviation of Brillouin zone. λ and $\mathbf{q}$ are phonon branch and wave vector, respectively. Total phonon relaxation time is obtained through Matthiessen's rule:

$$\tau_\lambda^{-1} = \tau_{iso,\lambda}^{-1} + \tau_{ph,\lambda}^{-1}, \tag{2}$$

in which isotope scattering rates and phonon-phonon scattering rates are given by Refs. [50–52]:

$$\tau_{iso,\lambda}^{-1} = \sum_{\lambda'} \Gamma_{\lambda\lambda'} = \frac{\pi\omega^2}{2} \sum_{\lambda'} \sum_i g(i) \left|e_\lambda^*(i)\cdot e_{\lambda'}(i)\right|^2 \delta(\omega_\lambda - \omega_{\lambda'}), \tag{3}$$

$$\tau_{ph,\lambda}^{-1} = \frac{1}{N}\left(\sum_{\lambda'\lambda''}^+ \Gamma_{\lambda\lambda'\lambda''}^+ + \sum_{\lambda'\lambda''}^- \frac{1}{2}\Gamma_{\lambda\lambda'\lambda''}^-\right), \tag{4}$$

where $g(i)$ is the Pearson deviation coefficient of the ith atom in the unit cell, e is the eigenvector. N is the number of $\mathbf{q}$ points. The transition probability matrix Γ denotes the probability of phonon scattering events, which is obtained from Fermi's golden rule [53]. In three phonon scattering, $\Gamma_{\lambda\lambda'\lambda''}^+$ and $\Gamma_{\lambda\lambda'\lambda''}^-$ represent two types of scattering events, combination process $\lambda + \lambda' \to \lambda''$ and splitting process $\lambda \to \lambda' + \lambda''$, respectively [53,54].

Here, first-principles calculation is carried out utilizing VASP package [55,56] to obtain the IFCs. Generalized gradient approximation (GGA) with the projector augmented-wave (PAW) method using Perdew-Burke-Ernzerhof (PBE) [57] form is applied for the exchange-correlation function. The energy cutoff of 500 eV is used. The electronic self-consistent loop and ionic relaxation loop stop while the total energy difference is below 10^{-8} eV and Hellmann-Feynman force difference is under 10^{-4} eV/Å. To correct the van der Waals (vdW) force, the Tkatchenko and Scheffler (DFT-TS) method is chosen, which has shown good agreement with the experimental data [36]. The $21 \times 21 \times 1$ Monkhorst-Pack [58] mesh is utilized for the structure relaxation of 2- to 5-layer Te and the $20 \times 20 \times 20$ for the bulk. Within density function theory (DFT), harmonic calculations are performed with the $8 \times 8 \times 1$ supercell for 2-layer tellurene, $6 \times 6 \times 1$ for 3-layer, 4-layer, and 5-layer tellurene, and $4 \times 4 \times 4$ for bulk tellurium, respectively. The PHONOPY [59] is used to extract the 2nd IFCs and plot phonon spectra. Temperature-dependent effective potential (TDEP) method [60] is employed to eliminate the tiny imaginary phonon frequency. The anharmonic calculations are carried out with the $8 \times 8 \times 1$ supercell for the 2-layer, $6 \times 6 \times 1$ for the 3-layer, $5 \times 5 \times 1$ for the 4-layer and 5-layer, and $4 \times 4 \times 4$ for the bulk. Cutoff radiuses in the DFT calculations are considered up to the eighth-nearest-neighbor atoms. THIRDORDER.PY [54] is used to extract third-order IFCs. The BTE is solved by ShengBTE [54] package, with the $130 \times 100 \times 1$, $170 \times 130 \times 1$, $120 \times 90 \times 1$, $110 \times 80 \times 1$, and $24 \times 24 \times 24$ q-grids for the 2-layer, 3-alyer, 4-layer, 5-layer, and bulk respectively after careful convergence test.

2.2. Monte Carlo simulation

Limited by the expensive computation, 5-layer Te, of which the unitcell contains 15 atoms, is the thickest 2D Te (though it may not be very rigorous to classify 5-layer Te into 2D materials, let us just tentatively accept it for convenience) that we can handle with the first-principles calculation. For the Te films with a thickness between the 5-layer and the bulk, a more appropriate choice is Monte Carlo (MC) simulation, which breaks the constraint of the huge number of atoms in the supercells and can easily enable the thickness effect by performing boundary scattering and controlling the size of the simulation domain. Therefore, MC simulation is applied to gain the in-plane thermal conductivities of the Te films with the thickness from 10 to 5000 nm in this work.

Our MC simulation bases on the energy variance-reduced formula of PBTE [61]:

$$\frac{\partial e_\lambda}{\partial t} + v_\lambda \nabla e_\lambda = \frac{e_\lambda^{loc} - e_\lambda}{\tau_\lambda}, \tag{5}$$

where $e = \hbar\omega f$ and $e^{loc} = \hbar\omega f^{loc}$ denote the real and pseudo energy. f and f^{loc} are the phonon distribution functions referring to the real temperature T and pseudo temperature T_{loc}, which can be obtained from these relations,

$$E = V \int_{\omega=0}^{\omega_{max}} \sum_\lambda \frac{D(\omega,\lambda)\hbar\omega}{\exp\left(\frac{\hbar\omega}{k_B T}\right) - 1} d\omega = N_{eff} \sum_i \hbar\omega_i, \tag{6}$$

$$\widetilde{E} = V \int_{\omega=0}^{\omega_{max}} \sum_\lambda \frac{D(\omega,\lambda)\hbar\omega}{\exp\left(\frac{\hbar\omega}{k_B T_{loc}}\right) - 1} d\omega = N_{eff} \sum_i \frac{\hbar\omega_i}{\tau(\omega_i, \lambda_i, T)}, \tag{7}$$

here, V is the volume of the simulation domain, D is the phonon density of states, and N_{eff} denotes the number of the effective phonons along the heat flux direction.

In the heat flux direction, *i.e.*, x direction in this system, periodic flux condition [61,62] is employed. The hot and cold walls are isothermal boundaries with the temperatures of 305 K and 295 K for the simulation at 300 K. Non-periodic diffusive scattering boundaries are applied in the thickness direction (z axis). In y direction, periodic specular scattering boundaries are adopted. N_b, the number of phonon particles emitted from the isothermal boundaries into the simulation domain is derived from these relations

$$N_b \varepsilon_{eff} = \frac{L_y L_z t_{step}}{N_q V_{pri}} \sum_{n=1}^{N_{ir}} \sum_\lambda \hbar\omega_{n,\lambda} \left|f^{eq}\left(\omega_{n,\lambda}, \lambda, T_b\right) - f^{eq}\left(\omega_{n,\lambda}, \lambda, T_{ref}\right)\right| \cdot \left|\sum_{G_n} v_x^{n,\lambda}\right|, \tag{8}$$

$$\varepsilon_{eff} = \frac{L_x L_y L_z}{N_{in} N_q V_{pri}} \sum_{n=1}^{N_{ir}} \sum_\lambda \hbar\omega_{n,\lambda} \left|f^{eq}\left(\omega_{n,\lambda}, \lambda, T\right) - f^{eq}\left(\omega_{n,\lambda}, \lambda, T_{ref}\right)\right| \cdot G_n, \tag{9}$$

where ε_{eff} denotes the effective average energy of each phonon particles. N_{in} is the number of phonons newly generated in the simulation domain during each time step. L_x, L_y, and L_z are the size of the simulation domain. N_q, N_{ir}, and V_{pri} are the number of all $\mathbf{q}$-points in the first Brillouin zone, the number of the irreducible $\mathbf{q}$-points in the first Brillouin zone, and the volume of primitive cell, respectively. G_n denotes the weighting factor of the irreducible q-points, *i.e.*, the number of $\mathbf{q}$-points corresponding to each irreducible $\mathbf{q}$-point, which satisfies the relation

$$N_q = \sum_{n=1}^{N_{ir}} G_n, \tag{10}$$

Phonon-phonon scattering, isotope scattering, and impurity scattering are considered in the simulation, given by Eq. (4), Eq. (3), and

$$\tau_{imp,\lambda}^{-1} = \frac{V_0 F \omega_\lambda^4}{4\pi v_\lambda^3}, \tag{11}$$

where V_0 is the volume per atom and F represents the strength of the scattering from the impurity [63–65]. The probability of the occurrence of phonon scattering during one time step t_{step} is given by

$$P_{sca,\lambda,\omega} = 1 - \exp\left(-\frac{t_{step}}{\tau_{\lambda,\omega}}\right), \tag{12}$$

In each phonon advection process, a random number R ranging from 0 to 1 is generated for each phonon particle. Phonon scattering happens when $R < P_{sca,\lambda,\omega}$. Another random number R_1 is generated to determine whether this phonon scattering is phonon-phonon scattering or not. It is phonon-phonon scattering when

$$R_1 < \frac{\tau_{ph,\lambda}^{-1}}{\tau_{ph,\lambda}^{-1} + \tau_{iso,\lambda}^{-1} + \tau_{imp,\lambda}^{-1}}, \tag{13}$$

otherwise, it is isotope or impurity scattering which are both elastic scattering. More theoretical details of our MC simulation can be found in Ref. [66].

As input of the MC simulation, the phonon dispersion and scattering rates of the bulk is acquired from the first-principles calculation. L_x and L_y are set to 500 and 100 nm, respectively. Thickness L_z ranges from 10 to 5000 nm. The N_{in} of 300 is chosen. The time step is set to 100 fs and the results converge after 5000 steps. The temperature profile and the thermal conductivity versus iteration steps is plotted in Fig. S1, which verifies the convergency of the MC simulation.

3. Results and discussion

Tellurium is composed of parallelly-stacking helical atom-chains along which the neighbor atoms is connected by covalent bonds (CBs), as shown in Fig. 1, while the atom-chains are linked by covalent-like quasi-bonding (CLQB) [27,37,67], a type of interaction whose strength is between normal vdW force and CBs, in the other two directions. Bulk Te belongs to P3₁21 space group, owning three-fold central symmetry along the c-axis. As a result, all Te atoms in bulk is equivalent. The a-c plane of the bulk is defined as in-plane in this work. Thus, separating specific layers along a-c plane from the bulk will result

in 2D Te with specific thickness. Fig. 1(e) exhibits the lattice structure after cutting 3 layers from the bulk. "One layer" is defined as the parallelly aligned atom-chains in the in-plane direction, which actually contains three atom-layers, as the magenta rectangle shows in Fig. 1(e). Hereafter in this paper, if not specially noted, "layer" represents chain layer, instead of atom layer. Apparently, in each layer, interactions between neighbor atoms are CBs in along-chain (AC) direction and CLQB in cross-chain (CC) direction, as shown in Fig. 1(d). The lattice constants of 2- to 5-layer and bulk Te after relaxation through first-principles calculation are listed in Table 1, from which it can be discovered that the lattice of Te expands gradually both in AC and CC directions from 2D to 3D. As a consequence, the distance between two neighbor atom-chains will grow and the CLQB will become weaker (this will be proved later).

Fig. 2 shows the thickness-dependent in-plane thermal conductivity of Te at 300 K from 2D to 3D. As aforementioned, our data of 2- to 5-layer and bulk Te is obtained from first principle PBTE method, and the results of the Te films with the thickness of 10–5000 nm are from MC simulation. All the values in this work are marked as solid stars in Fig. 2. The theoretical values of monolayer Te (β-phase) and experimental data of the Te films and bulk are from Refs. [25,42,47,68], which is plotted as hollow scatters in Fig. 2. It is worth noting that we take monolayer β-Te instead of α-Te or γ-Te among the most stable phases of Te for reference because monolayer α-Te is not stable and the β-phase has more similar structure to the α-phase than the γ-phase does [35,37]. Monolayer β-Te can be transformed into from monolayer α-Te (which is not stable) by compressing along CC direction [35]. The only difference between these two phases is that the CLQBs in CC direction turns into CBs due to the closer distance between neighbor atom-chains, which makes the comparison reasonable. By contrast, monolayer γ-Te [35] is closer to the structure of 1T-MoS₂ [69], which has lost the helical atom-chain

Table 1
The lattice constants of the few-layer tellurene and the bulk tellurium after structure optimization by first-principles calculation.

Lattice constants (Å)	2-layer	3-layer	4-layer	5-layer	bulk
a (CC)	4.328	4.362	4.377	4.385	4.509
b (AC)	5.782	5.837	5.861	5.874	5.959
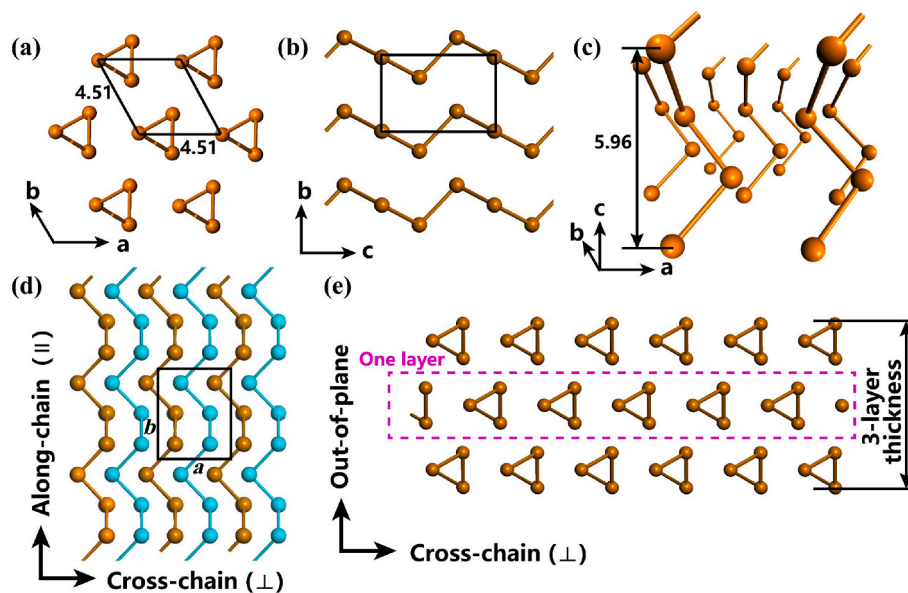
Fig. 1. The lattice structure of bulk Te on the top view (a), the side view (b), and the perspective view (c). And the lattice structure of 3-layer Te on the in-plane view (d) and the side view (e). Black solid rectangles label the unitcells. The magenta dashed rectangle in (e) separates one layer of Te. Noteworthy is that the different colors of Te atoms in (d) is aimed to show the neighbor Te layers, it does not mean they are different type of atoms.
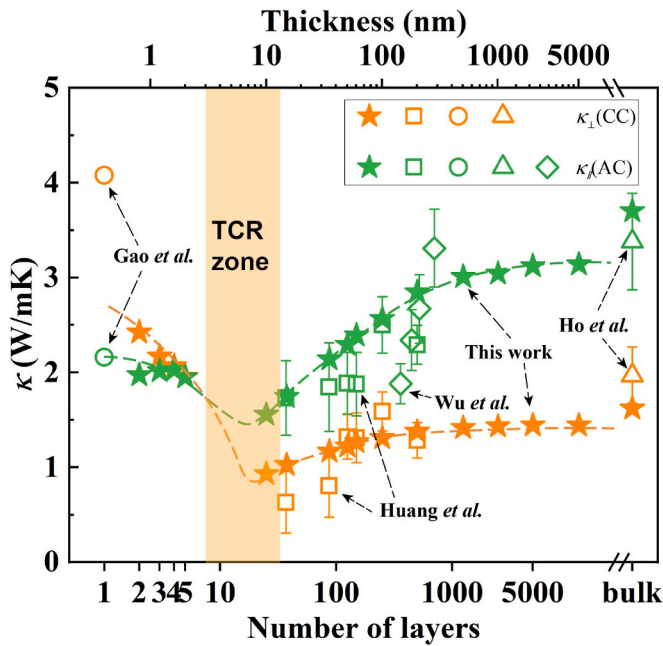
Fig. 2. Thermal conductivity of Te at room temperature versus thickness (number of layers). Orange and green scatters are the values in CC (⊥) and AC (∥) directions, respectively. Solid stars are the data in this work, hollow circles are the theoretical values of monolayer β-Te from first-principles calculation [42], hollow squares are the experimental results of Te films with the thickness ranging from 15 to 200 nm [25], hollow rhombuses are the experimental $\kappa_\parallel$ of the Te nanoribbons with the thickness of 144, 179, 209, and 281 nm [68], and hollow triangles are the experimental thermal conductivities of bulk Te [47]. The dashed curves are tendency lines added manually. The orange area is the expected TCR zone where the thermal conductivities reach their minimum. The data from MC simulation of this work are obtained with the impurity fraction of 0.01% taken into consideration.

structure. Therefore, comparing γ-phase with α-phase is pointless to the evolution of in-plane heat transport in Te. With the isotope and impurity scattering involved, our MC simulation results agree well with the data from TDTR measurements [25]. As well, the bulk Te data from our first-principles calculation has a reasonably good agreement with the experimental results. The deviation of our MC simulation results and the experimental values from Huang et al. (hollow squares in Fig. 2, thickness ranging from 15 to 200 nm) shows some fluctuation, i.e., the simulation overestimates or underestimates at different thickness, though within acceptable tolerance. We owe this to the uncontrollable impurity fraction of the experimental samples, in contrast to the fixed impurity fractions of 0.01% in the MC simulation. With regard to the deviation between the theoretical values and the experimental measurements from Wu et al. (hollow rhombuses in Fig. 2), except for the uncontrollable impurity fraction, we believe it also stems from the phonon-boundary scattering in the nanoribbons of which the MFP-comparable width ranges from 554 to 968 nm [68], by contrast to the infinite width (periodic boundary) in our MC simulation. To the best of our knowledge, there is no reported experimental data of the Te films thinner than 15 nm yet due to the challenging fabrication and measurement of the ultra-thin tellurene. The orange and green tendency lines in Fig. 2 represent the development of the thermal conductivity from 2D to 3D. The thermal conductivities in CC and AC direction have the analogous non-monotonic trend. When thickness increases from monolayer to bulk, $\kappa_\perp$ and $\kappa_\parallel$ both fall first and then rise. We signature this non-monotonic dependence as "Thermal conductivity rebound" (TCR). The expected bottoms of these two tendency lines appear between 6-layer and ~15-layer, which is highlighted as TCR zone in Fig. 2, with the lowest thermal conductivity of ~0.88 and ~1.45 W/mK in CC

and AC direction, respectively. The critical thickness corresponding to the lowest thermal conductivity is determined by the deviation of 2D phonon transport in very thin films (~10 nm) from the 3D phonon transport in bulk [29], as shown in Fig. S4. On the left side of the TCR zone, $\kappa_\perp$ is higher than $\kappa_\parallel$ at the beginning (2.42 W/mK of $\kappa_\perp$ and 1.97 W/mK of $\kappa_\parallel$ for 2-layer Te) and has a steeper slope than that of $\kappa_\parallel$, resulting in the surpass of the $\kappa_\parallel$. On the right side of TCR zone, $\kappa_\parallel$ has a higher speed of ascent than $\kappa_\perp$ with the enhancing thickness, and they both stop rising at around 5000-layer.

Thermal anisotropy is another important feature of phonon transport. In order to explore the evolution of the in-plane thermal anisotropy of Te from 2D to 3D, anisotropy ratio (AR = $\kappa_\perp/\kappa_\parallel$) of Te versus thickness is exhibited in Fig. 3. It is universally acknowledged that in layered vdW crystals, the in-plane or AC thermal conductivity is larger than the out-of-plane or CC thermal conductivity, owing to the weaker strength of vdW force in the out-of-plane or CC directions than that of CBs in the in-plane or CC directions. In other words, it is normal that ARs of layered materials are lower than 1, while an AR higher than 1 is abnormal. Our prior work found the first case of abnormal AR in bilayer tellurene [27]. As a follow-up, now in this work, we discover that 2- to 5-layer Te all have an abnormal thermal anisotropy (AR > 1), as shown in Fig. 3. With the increasing number of layers, the AR of Te gradually reduces from 1.889, the AR of monolayer Te, to 1.003, the AR of 5-layer Te, then it falls below the isotropic line (AR = 1), and finally reaches 0.438, the AR of bulk Te. The highlighted region shows the predicted location where the thermal anisotropy reverses from abnormal to normal, which is named "thermal anisotropy reversal" (TAR) zone. The guessed reversal point appears around 7-layer (~2.5 nm), according to the intersection of the AR tendency line and the isotropic line. On the right side of TAR zone, AR of Te consistently stays lower than 1. According to the reported studies to date, the ARs of in-plane anisotropic layered materials do not reverse with various thicknesses, in other words, their in-plane anisotropy is thickness independent. As Fig. 3 shows, the ARs of BP [15,20,70], WTe₂ [22,71], PdSe₂ [72], and TiS₃ [24] all stay below 1, not crossing the isotropy line at different thicknesses. The TAR in Te is discovered for the first time among in-plane anisotropic 2D materials.
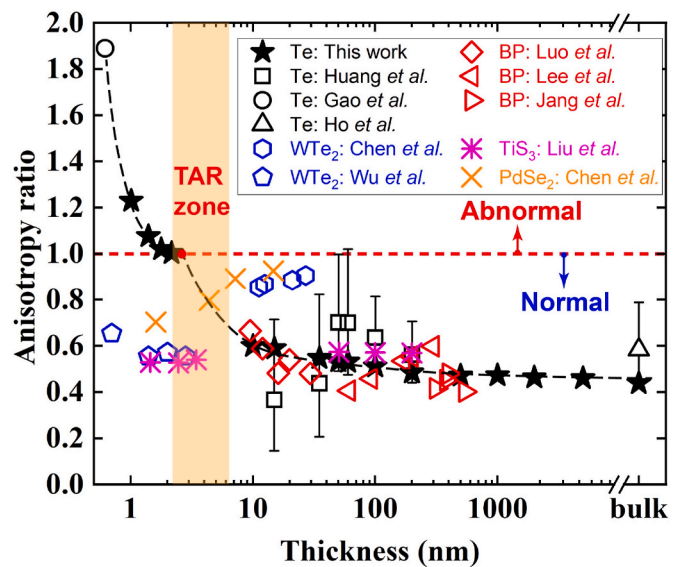
Fig. 3. Thermal anisotropy ratio (AR, $\kappa_\perp/\kappa_\parallel$) of Te at RT as a function of thickness, in comparison with other 2D materials. Black, red, blue, magenta, and orange symbols are the data of Te [25,42,47], BP [15,20,70], WTe₂ [22,71], TiS₃ [24], and PdSe₂ [72], respectively. AR is defined as $\kappa_{armchair}/\kappa_{zigzag}$ for BP and WTe₂, $\kappa_{a-axis}/\kappa_{b-axis}$ for TiS₃ and PdSe₂. The black dashed line is added manually to guide the trend of the AR of Te. The red dashed reference line is the isotropy line. The red intersection point of the dashed lines refers to the expected thickness where the TAR occurs.

In prior studies [23,24,28,29,48,73], the thickness dependences of thermal transport in 2D materials are attributed to the change of phonon dispersion, phonon density of states, phonon group velocity, relaxation time, phonon confinement, and phonon transport regimes. Though in different framework, phonon confinement [29,48,49] and phonon transport regimes [73] both refer to the correlation between film thickness and phonon mean free path, which is determined by phonon velocity and relaxation time. Therefore, these factors can be concluded as phonon transport properties. In this work, except analyzing frequency-dependent, mode-dependent, and direction-dependent phonon transport properties, we will furtherly explore the origin of the change of phonon transport properties. TCR and TAR phenomena in Te triggered by dimension transition will be explained in the rest of this paper.

Phonon group velocity and relaxation time are positively correlated to thermal conductivity, according to Eq. (1). To visibly illustrate the influence of phonon group velocity and relaxation time, the frequency-resolved average phonon group velocity $\bar{v}$ and relaxation time $\bar{\tau}$ of 2- to 5-layer and bulk are displayed in Fig. 4. The original phonon group velocity, phonon relaxation time, and the derivation of $\bar{v}$ and $\bar{\tau}$ are given in Fig. S2 and the corresponding notes. The average group velocity shows different dependence of thickness at different frequency range, as shown in Fig. 4(a). When the number of layers enhances from 2-layer to bulk, in the range of very low frequency (<0.4 THz), the average group
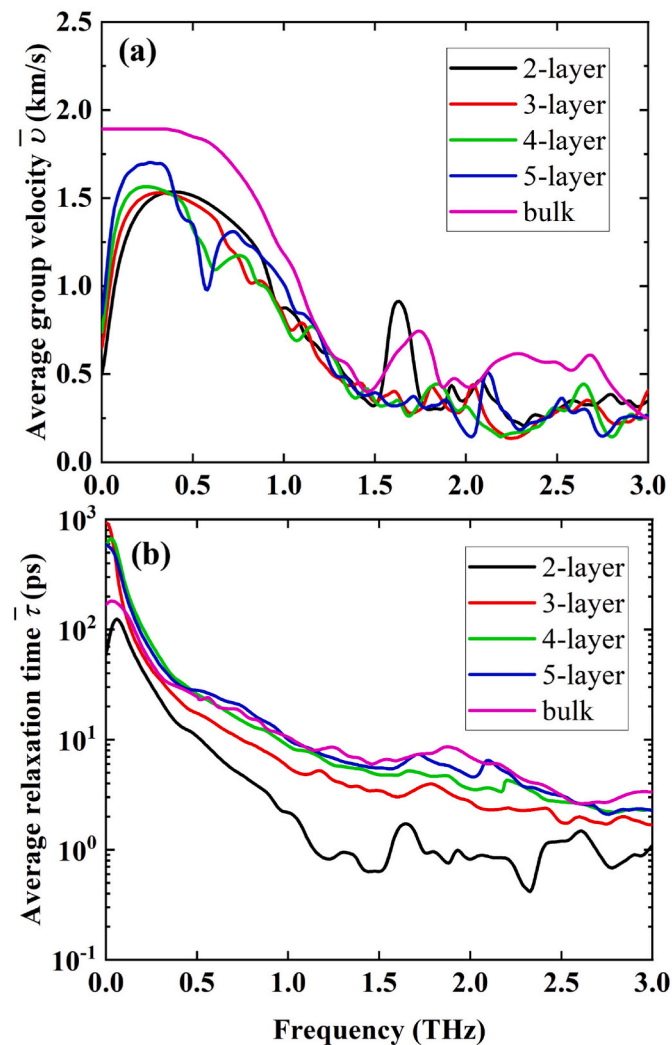
velocity monotonically rises up; in the rest of the frequency range, $\bar{v}$ shows the similar non-monotonic development with the in-plane thermal conductivity, *i.e.*, first reducing and then rising. Interestingly, in the range of 1.5–1.75 THz, the average of group velocity of 2-layer Te is the highest, while the bulk dominates in other frequency range, implying that the phonons with the frequency from 1.5 to 1.75 THz are important in the thermal transport of 2D Te. The overall non-monotonic dependence of the group velocity accords with the trend of the in-plane thermal conductivities, demonstrating that the non-monotonic group velocity is the main reason of the TCR. On the other hand, average phonon relaxation time basically keeps ascending with the number of layers, as Fig. 4(b) shows. This indicates that before the TCR zone (very thin 2D Te), relaxation time is the minor factor and group velocity is the major factor that influences the thermal conductivity so that the thermal conductivities keep falling before the TCR zone. After TCR zone, phonon relaxation time and group velocity both contribute to the enhancement of the thermal conductivities.

In order to explore the origin of the TAR, the directional average group velocities and the cumulative thermal conductivities versus frequency are exhibited in Fig. 5. The frequency range in Fig. 5 are only up to 3.0 THz because all the cumulative thermal conductivities stop rising before 3.0 THz, namely, only the phonons between 0.0 and 3.0 THz contribute to the thermal conductivity. In 2-layer Te (Fig. 5(a)), the average $v_\perp$ is overall higher than $v_\parallel$. Especially, there is a big gap between them at the frequency range of LFO phonons (1–2 THz). This is why 2-layer Te has an abnormal AR ($\kappa_\perp > \kappa_\parallel$). By sharp contrast, in bulk Te (Fig. 5(e)), $v_\perp$ is lower than $v_\parallel$ through the whole frequency range, resulting in a normal AR. When the thickness increases from 2-layer to 5-layer, the gap between $v_\perp$ and $v_\parallel$ gradually shortens but $v_\perp$ still keeps higher than $v_\parallel$, especially in the frequency range of 1.0–2.0 THz where the cumulative thermal conductivities are rising. It can be anticipated that from 5-layer to bulk Te, $v_\perp$ will keep reducing and will be exceeded by $v_\parallel$ at the predicted TAR point, around 7-layer, and then the discrepancy between them will enlarge again with $v_\perp$ below $v_\parallel$, leading to the continuing decreasing AR. It can be concluded that the development of the AR of Te originates from the change of the $v_\perp$ and the $v_\parallel$. The TAR occurs because $v_\perp$ that is higher than $v_\parallel$ at the beginning keeps falling fast while the $v_\parallel$ first reduces slightly and then enhances with the number of layers. Further origin of the development of the $v_\perp$ and $v_\parallel$ will be discussed later.

Part phonon dispersion and phonon density of states (PDOS) are shown in Fig. 6. The full phonon dispersion is given in Fig. S3. From 2-layer to 5-layer, the low-frequency optical (LFO, ~0.5–2 THz) branches and the intersections between these branches increases gradually, and the gap between LFO and acoustic phonons narrows, which indicates that phonon scattering channels increases and the acoustic-optical interaction (which is also known as phonon scattering between acoustic phonons and the LFO phonons) is reinforced. From 5-layer to bulk, the number of LFO branches reduces and the acoustic-optical branch gap broadens, implying the weakened acoustic-optical interaction. Since stronger acoustic-optical interaction means higher phonon scattering possibility, which will promote the generation of optical phonons from the combination of acoustic phonons and tends to lower down the thermal conductivity, the non-monotonic development of acoustic-optical interaction thus contributes to the up-to-down trend of the thermal conductivity. PDOS of the LFO phonons demonstrates this trend. With the increasing number of layers, PDOS of LFO phonons rises from 2- to 5-layer, and falls from 5-layer to bulk, as Fig. 6 (f) shows. The increasing number of LFO phonons can elevates the contribution of optical phonons to the thermal conductivity. Thus, the contributions of optical phonons to the $\kappa_\perp$ and $\kappa_\parallel$ both first rise up and then reduce with the thickness of Te, as shown in Fig. 7. The percentage of optical branches even reaches 41% and 42% in the contribution to $\kappa_\perp$ and $\kappa_\parallel$, respectively. The non-monotonically varying contribution of optical branches reflects the important role of LFO phonons on the in-plane heat transport in 2D Te. More specifically, the LFO phonons affect the heat
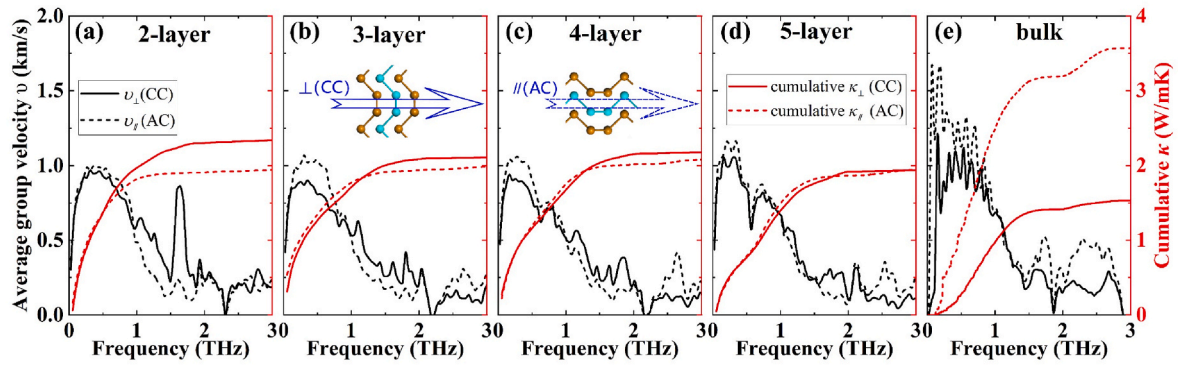

Fig. 4. Frequency-resolved average phonon group velocity (a) and relaxation time at 300 K (b).

Fig. 5. Frequency-resolved directional average phonon group velocity (black lines) and the cumulative thermal conductivity (red lines) of 2- to 5-layer (a–d) and bulk (e) Te. The solid and dashed lines respectively correspond to the CC and AC direction, as the insets in (b) and (c) shows.
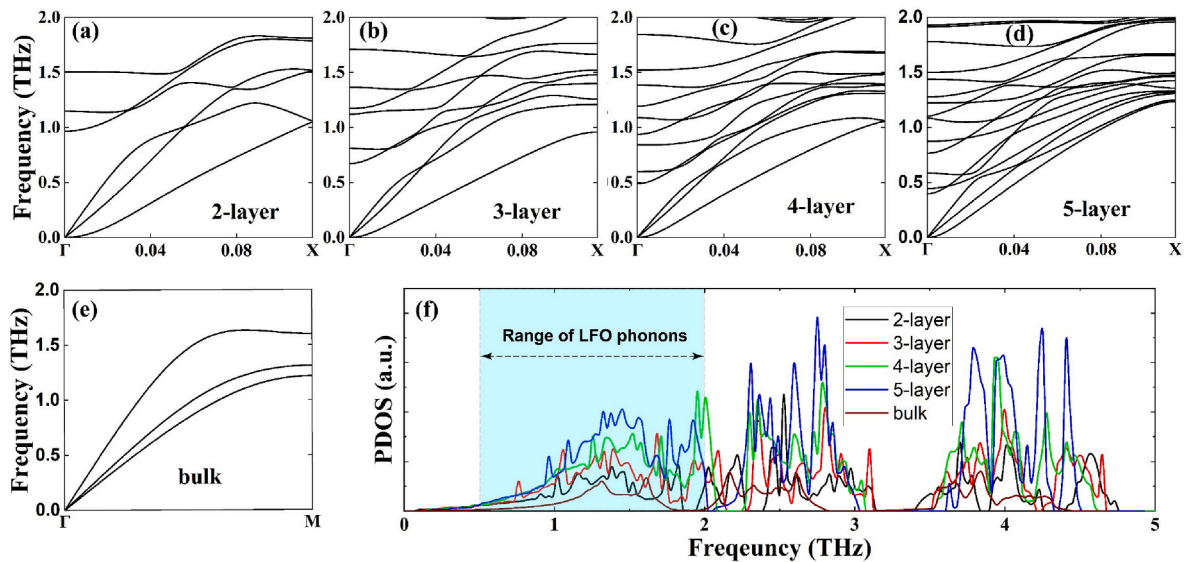

Fig. 6. Part phonon dispersions (a–e) and phonon density of states (PDOS) (f) of 2- to 5-layer and bulk Te.

transport in two aspects: (1) the group velocity of LFO phonons is the primary factor that contributes to the TCR and TAR, as discussed in the last two paragraph; (2) the existence of LFO phonons promotes the phonon scattering, which tends to shorten phonon relaxation time, thus higher density of LFO phonons tends to lower down the thermal conductivity.

Size effect, or thickness effect, is critical to the in-plane thermal transport in 2D materials. Fu et al. [29] and Liu et al. [24] explained the non-monotonic heat transport in silicon, argon, and TiS$_3$ films through the concept of phonon confinement, which is essentially also thickness effect. When the size of the thin film is comparable with the phonon mean free path (MFP), the impact of boundary scattering will grow, and impede the phonon transport. To explore the influence of the thickness effect, we calculate the MFP and the normalized cumulative thermal conductivities as a function of MFP, as shown in Fig. 8. The MFP ranges of different Te films/bulk are basically the same, from 10^{-1} to 10^3 nm, while the sensitivities of their thermal conductivity to MFP are different. Fig. 8 (b) and (c) show the normalized cumulative $\kappa_\perp$ and $\kappa_\parallel$. The two reference lines at 0.75 and 1.0 are marked to measure the sensitivity to MFP. The curve reaching the reference lines earlier is less sensitive to MFP. Apparently, the sensitivities to MFP of $\kappa_\perp$ and $\kappa_\parallel$ both decrease with the thickness. In other words, when the thickness of Te increases, the thickness effect gradually declines. If only considering the thickness effect, the in-plane thermal conductivities should monotonically increase with the thickness. However, when the thickness is lower than the

TCR zone, the LFO phonons have strong impact on the in-plane thermal transport. The group velocity of LFO phonons falls down with the thickness, which dominates in affecting the thermal conductivity and leads to the negative thickness dependence of $\kappa_\perp$ and $\kappa_\parallel$ at the left side of TCR zone. Summing up the above analyses, the combined effect of LFO phonons and thickness effect is the ultimate factor that leads to the TCR and TAR in Te.

As is well known, phonon is the quantum form of lattice vibration, which is affected by the strength of interatomic forces. For the case of Te, in CC direction the interaction is CLQB and in AC direction CB. In order to investigate further physics behind the evolution of the in-plane thermal transport of Te, the integrated crystal orbital Hamilton populations (ICOHPs) [74] in CC and AC direction of Te–Te atom pair are given in Fig. 9. The negative ICOHP near the Fermi level represents bonding states while the positive ICOHP denotes anti-bonding states. Higher absolute value of ICOHP means stronger intensity of the bonding or anti-bonding states. At the Fermi level, the absolute ICOHP in CC direction reduces with the thickness, according to Fig. 9 (a), which indicates that the CLQB in CC direction is weakened gradually. In comparison, the CB in AC direction is first weakened and then strengthened, as shown in Fig. 9 (b). Of note is that the ICOHP of the 5-layer is not accessible because the calculation is beyond our current computation capability. As is shown in Table 1, from the 2-layer to bulk Te, the lattice constants are monotonically increasing, which means the atomic distance is enlarged in both CC and AC direction with the number of layers.
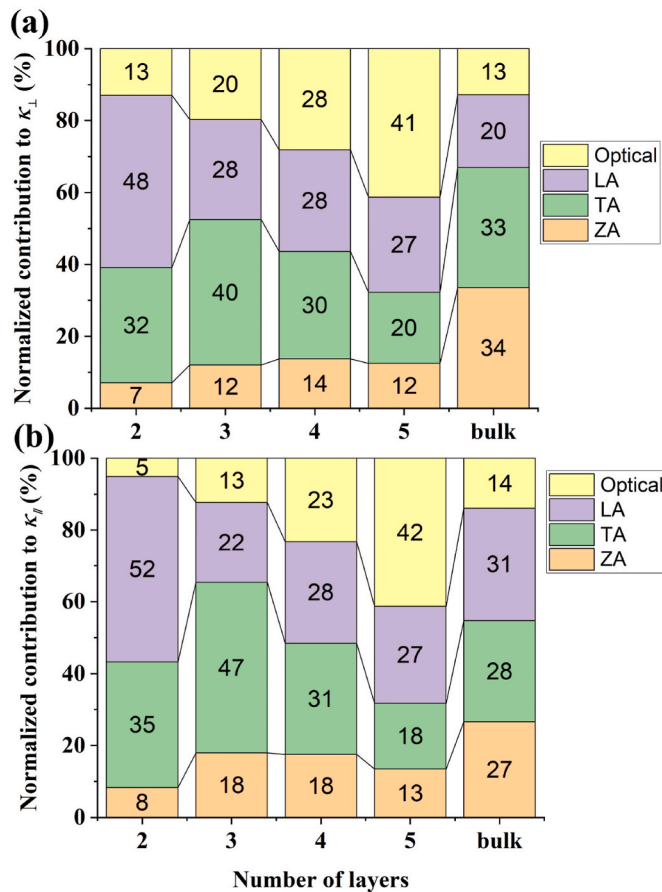
Fig. 7. The normalized contribution of different phonon branches to $\kappa_\perp$ (a) and $\kappa_\parallel$ (b) at 300 K versus number of layers.

The different dependence of CLQB and CB on the atomic distance can be understood by the following analogy: imaging covalent bond as a coil spring, if the coil spring is pressed at the beginning (2-layer), with the stretching (atomic distance is enlarged), the strength of the elastic force will decrease before the coil spring reaching the equilibrium length and increase after that point; as for CLQB, we can image it as a coil spring that is already cracked under excessive stretching at the beginning (2-layer), with continual stretching, the connection intensity will become weaker and weaker. The gradual decline of the CLQB will soften the LFO phonons in CC direction, resulting in the reducing $v_\perp$. Similarly, in AC direction, the non-monotonically changing CB leads to the $v_\parallel$ first decreasing and then rising as the thickness increases (Fig. 5). Therefore, the root of the development of LFO phonons properties is the lattice expansion and the subsequent decline of the CLQB in CC direction.

4. Conclusion

In summary, using first principle PBTE method and MC simulation, we predicted the in-plane thermal conductivities in CC and AC directions of Te with various thickness, and demonstrated a full picture of the in-plane thermal evolution in Te from 2D to 3D. A unique combination of thermal conductivity rebound and thermal anisotropy reversal are discovered, the origin of which is attributed to the interplay effect of LFO phonons and thickness effect. The LFO phonons affect the in-plane heat transport through its non-monotonically evolving group velocity and the changing phonon scattering rates. The evolution of LFO phonon properties with increasing thickness originate from the lattice expansion, which diminishes CLQB.
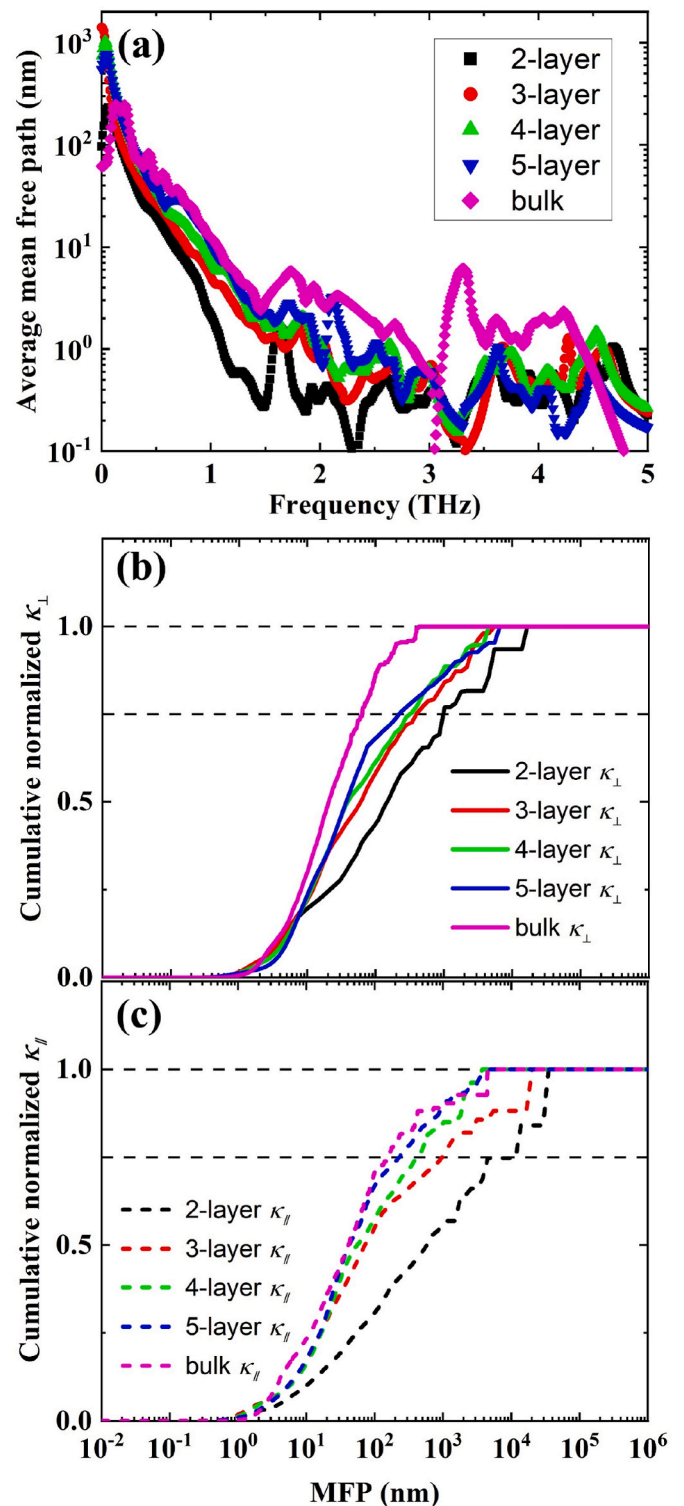

Fig. 8. Frequency-resolved average MFP (a), the cumulative normalized RT $\kappa_\perp$ (b), and the cumulative normalized RT $\kappa_\parallel$ (c) versus MFP of Te with various thickness.

Author statement

Yanhua Cheng: Conceptualization, Investigation, Data curation, Visualization, Writing-Original draft preparation; **Jinlong Ma**: Methodology, Formal analysis, Writing-Review and editing; **Yaxin Xu**: Methodology, Validation; **Guoqing Sun**: Methodology, Validation; **Xiulin Ruan**: Writing-Review and editing, Supervision; **Xiaobing Luo**:
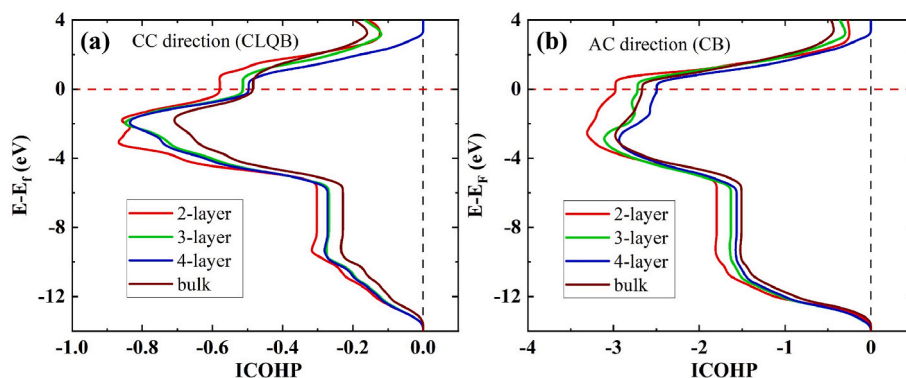
Fig. 9. Integrated COHP of the Te–Te interaction along CC (a) and AC (b) directions in Te with different thickness.

Supervision, Funding acquisition.

Declaration of competing interest

The authors declare that they have no known competing financial interests or personal relationships that could have appeared to influence the work reported in this paper.

Acknowledgement

Appendix A. Supplementary data

Supplementary data to this article can be found online at https://doi.org/10.1016/j.mtphys.2022.100776.

References

[1] K.S. Novoselov, A.K. Geim, S.V. Morozov, D. Jiang, Y. Zhang, S.V. Dubonos, I.V. Grigorieva, A.A. Firsov, Electric field effect in atomically thin carbon films, Science 306 (2004) 666–669, https://doi.org/10.1126/science.1102896.

[2] A.K. Geim, K.S. Novoselov, The rise of graphene, Nat. Mater. 6 (2007) 183–191, https://doi.org/10.1038/nmat1849.

[3] T. Kambe, S. Imaoka, M. Shimizu, R. Hosono, D. Yan, H. Taya, M. Katakura, H. Nakamura, S. Kubo, A. Shishido, K. Yamamoto, Liquid crystalline 2d borophene oxide for inorganic optical devices, Nat. Commun. 13 (2022) 1037, https://doi.org/10.1038/s41467-022-28625-w.

[4] E. Piatti, A. Arbab, F. Galanti, T. Carey, L. Anzi, D. Spurling, A. Roy, A. Zhussupbekova, K.A. Patel, J.M. Kim, D. Daghero, R. Sordan, V. Nicolosi, R.S. Gonnelli, F. Torrisi, Charge transport mechanisms in inkjet-printed thin-film transistors based on two-dimensional materials, Nat. Electron. 4 (2021) 893–905, https://doi.org/10.1038/s41928-021-00684-9.

[5] P.R. Kidambi, P. Chaturvedi, N.K. Moehring, Subatomic species transport through atomically thin membranes: present and future applications, Science 374 (2021): eabd7687, https://doi.org/10.1126/science.abd7687.

[6] C. Chang, M. Wu, D. He, Y. Pei, C.F. Wu, X. Wu, H. Yu, F. Zhu, K. Wang, Y. Chen, L. Huang, J.F. Li, J. He, L.D. Zhao, 3d charge and 2d phonon transports leading to high out-of-plane zt in n-type snse crystals, Science 360 (2018) 778–783, https://doi.org/10.1126/science.aaq1479.

[7] F. Bonaccorso, L. Colombo, G. Yu, M. Stoller, V. Tozzini, A.C. Ferrari, R.S. Ruoff, V. Pellegrini, 2d materials. Graphene, related two-dimensional crystals, and hybrid systems for energy conversion and storage, Science 347 (2015): 1246501, https://doi.org/10.1126/science.1246501.

[8] S.-Y. Seo, J. Park, J. Park, K. Song, S. Cha, S. Sim, S.-Y. Choi, H.W. Yeom, H. Choi, M.-H. Jo, Writing monolithic integrated circuits on a two-dimensional semiconductor with a scanning light probe, Nat. Electron. 1 (2018) 512–517, https://doi.org/10.1038/s41928-018-0129-6.

[9] Q. Cai, D. Scullion, W. Gan, A. Falin, S. Zhang, K. Watanabe, T. Taniguchi, Y. Chen, E.J.G. Santos, L.H. Li, High thermal conductivity of high-quality monolayer boron nitride and its thermal expansion, Sci. Adv. 5 (2019) https://doi.org/10.1126/sciadv.aav0129 eaav0129.

[10] C. Yuan, J. Li, L. Lindsay, D. Cherns, J.W. Pomeroy, S. Liu, J.H. Edgar, M. Kuball, Modulating the thermal conductivity in hexagonal boron nitride via controlled boron isotope concentration, Commun. Phys. 2 (2019), https://doi.org/10.1038/s42005-019-0145-5.

[11] L. Lindsay, D.A. Broido, Theory of thermal transport in multilayer hexagonal boron nitride and nanotubes, Phys. Rev. B 85 (2012), https://doi.org/10.1103/PhysRevB.85.035436.

[12] A.N. Gandi, U. Schwingenschlögl, Thermal conductivity of bulk and monolayer mos2, EPL 113 (2016), https://doi.org/10.1209/0295-5075/113/36002.

[13] Y. Cai, J. Lan, G. Zhang, Y.-W. Zhang, Lattice vibrational modes and phonon thermal conductivity of monolayer mos2, Phys. Rev. B 89 (2014), https://doi.org/10.1103/PhysRevB.89.035438.

[14] R. Yan, J.R. Simpson, S. Bertolazzi, J. Brivio, M. Watson, X. Wu, A. Kis, T. Luo, A.R. Hight Walker, H.G. Xing, Thermal conductivity of monolayer molybdenum disulfide obtained from temperature-dependent Raman spectroscopy, ACS Nano 8 (2014) 986–993, https://doi.org/10.1021/nn405826k.

[15] Z. Luo, J. Maassen, Y. Deng, Y. Du, R.P. Garrelts, M.S. Lundstrom, P.D. Ye, X. Xu, Anisotropic in-plane thermal conductivity observed in few-layer black phosphorus, Nat. Commun. 6 (2015), https://doi.org/10.1038/ncomms9572.

[16] A. Carvalho, M. Wang, X. Zhu, A.S. Rodin, H. Su, A.H. Castro Neto, Phosphorene: from theory to applications, Nat. Rev. Mater. 1 (2016), https://doi.org/10.1038/natrevmats.2016.61.

[17] X.-S. Wu, W.-T. Tang, X.-F. Xu, Recent progresses of thermal conduction in two-dimensional materials, Acta Phys. Sin. 69 (2020), https://doi.org/10.7498/aps.69.20200709.

[18] S. Ghosh, W. Bao, D.L. Nika, S. Subrina, E.P. Pokatilov, C.N. Lau, A.A. Balandin, Dimensional crossover of thermal transport in few-layer graphene, Nat. Mater. 9 (2010) 555–558, https://doi.org/10.1038/nmat2753.

[19] D.L. Nika, A.A. Balandin, Phonons and thermal transport in graphene and graphene-based materials, Rep. Prog. Phys. 80 (2017): 036502, https://doi.org/10.1088/1361-6633/80/3/036502.

[20] H. Jang, J.D. Wood, C.R. Ryder, M.C. Hersam, D.G. Cahill, Anisotropic thermal conductivity of exfoliated black phosphorus, Adv. Mater. 27 (2015) 8017–8022, https://doi.org/10.1002/adma.201503466.

[21] S.G. Jeon, H. Shin, Y.H. Jaung, J. Ahn, J.Y. Song, Thickness-dependent and anisotropic thermal conductivity of black phosphorus nanosheets, Nanoscale 10 (2018) 5985–5989, https://doi.org/10.1039/c8nr00421h.

[22] C. Wu, C. Liu, Y. Tao, Y. Zhang, Y. Chen, Anomalous layer thickness dependent thermal conductivity of td-wte2 through first-principles calculation, Phys. Lett. 384 (2020) 1–8, https://doi.org/10.1016/j.physleta.2020.126751.

[23] X. Gu, B. Li, R. Yang, Layer thickness-dependent phonon properties and thermal conductivity of mos2, J. Appl. Phys. 119 (2016), https://doi.org/10.1063/1.4942827.

[24] C. Liu, P. Lu, D. Li, Y. Zhao, M. Hao, Non-monotonic thickness dependent and anisotropic in-plane thermal transport in layered titanium trisulphide, Material. Today Nano (2021), https://doi.org/10.1016/j.mtnano.2021.100165.

[25] S. Huang, M. Segovia, X. Yang, Y.R. Koh, Y. Wang, P.D. Ye, W. Wu, A. Shakouri, X. Ruan, X. Xu, Anisotropic thermal conductivity in 2d tellurium, 2D Mater. 7 (2019), https://doi.org/10.1088/2053-1583/ab4eee.

[26] W.-R. Zhong, M.-P. Zhang, B.-Q. Ai, D.-Q. Zheng, Chirality and thickness-dependent thermal conductivity of few-layer graphene: a molecular dynamics study, Appl. Phys. Lett. 98 (2011), https://doi.org/10.1063/1.3567415.

[27] Y. Cheng, X. Yang, Z. Han, W. Wu, X. Luo, X. Ruan, Abnormal in-plane thermal conductivity anisotropy in bilayer α-phase tellurene, Int. J. Heat Mass Tran. 192 (2022) 1–8, https://doi.org/10.1016/j.ijheatmasstransfer.2022.122908.

[28] B. Qiu, X. Ruan, Thermal conductivity prediction and analysis of few-quintuple bi2te3 thin films: a molecular dynamics study, Appl. Phys. Lett. 97 (2010), https://doi.org/10.1063/1.3514252.

[29] B. Fu, K.D. Parrish, H.-Y. Kim, G. Tang, A.J.H. McGaughey, Phonon confinement and transport in ultrathin films, Phys. Rev. B 101 (2020), https://doi.org/10.1103/PhysRevB.101.045417.

[30] Y. Dong, B. Zeng, X. Zhang, D. Li, J. He, M. Long, Study on the strain-induced mechanical property modulations in monolayer tellurene, J. Appl. Phys. 125 (2019), https://doi.org/10.1063/1.5079934.

[31] X. Cai, Y. Ren, M. Wu, D. Xu, X. Luo, Strain-induced phase transition and giant piezoelectricity in monolayer tellurene, Nanoscale 12 (2020) 167–172, https://doi.org/10.1039/c9nr06507e.

[32] J. Ma, F. Meng, J. He, Y. Jia, W. Li, Strain-induced ultrahigh electron mobility and thermoelectric figure of merit in monolayer α-te, ACS Appl. Mater. Interfaces 12 (2020) 43901–43910, https://doi.org/10.1021/acsami.0c10236.

[33] K.V. Sopiha, O.I. Malyi, C. Persson, First-principles mapping of the electronic properties of two-dimensional materials for strain-tunable nanoelectronics, ACS Appl. Nano Mater. 2 (2019) 5614–5624, https://doi.org/10.1021/acsanm.9b01164.

[34] Y. Wang, S. Yao, P. Liao, S. Jin, Q. Wang, M.J. Kim, G.J. Cheng, W. Wu, Strain-engineered anisotropic optical and electrical properties in 2d chiral-chain tellurium, Adv. Mater. 32 (2020): e2002342, https://doi.org/10.1002/adma.202002342.

[35] Y. Xiang, S. Gao, R.-G. Xu, W. Wu, Y. Leng, Phase transition in two-dimensional tellurene under mechanical strain modulation, Nano Energy 58 (2019) 202–210, https://doi.org/10.1016/j.nanoen.2019.01.040.

[36] Y. Wang, C. Xiao, M. Chen, C. Hua, J. Zou, C. Wu, J. Jiang, S.A. Yang, Y. Lu, W. Ji, Two-dimensional ferroelectricity and switchable spin-textures in ultra-thin elemental te multilayers, Mater. Horiz. 5 (2018) 521–528, https://doi.org/10.1039/c8mh00082d.

[37] J. Qiao, Y. Pan, F. Yang, C. Wang, Y. Chai, W. Ji, Few-layer tellurium: one-dimensional-like layered elementary semiconductor with striking physical properties, Sci. Bull. 63 (2018) 159–168, https://doi.org/10.1016/j.scib.2018.01.010.

[38] L. Tong, X. Huang, P. Wang, L. Ye, M. Peng, L. An, Q. Sun, Y. Zhang, G. Yang, Z. Li, F. Zhong, F. Wang, Y. Wang, M. Motlag, W. Wu, G.J. Cheng, W. Hu, Stable mid-infrared polarization imaging based on quasi-2d tellurium at room temperature, Nat. Commun. 11 (2020) 2308, https://doi.org/10.1038/s41467-020-16125-8.

[39] J.K. Qin, P.Y. Liao, M.W. Si, S.Y. Gao, G. Qiu, J. Jian, Q.X. Wang, S.Q. Zhang, S. Y. Huang, A. Charnas, Y.X. Wang, M.J. Kim, W.Z. Wu, X.F. Xu, H.Y. Wang, L. Yang, Y.K. Yap, P.D.D. Ye, Raman response and transport properties of tellurium atomic chains encapsulated in nanotubes, Nat. Electron. 3 (2020) 141–147, https://doi.org/10.1038/s41928-020-0365-4.

[40] S. Lin, W. Li, Z. Chen, J. Shen, B. Ge, Y. Pei, Tellurium as a high-performance elemental thermoelectric, Nat. Commun. 7 (2016): 10287, https://doi.org/10.1038/ncomms10287.

[41] Y. Wang, G. Qiu, R. Wang, S. Huang, Q. Wang, Y. Liu, Y. Du, W.A. Goddard, M. J. Kim, X. Xu, P.D. Ye, W. Wu, Field-effect transistors made from solution-grown two-dimensional tellurene, Nat. Electron. 1 (2018) 228–236, https://doi.org/10.1038/s41928-018-0058-4.

[42] Z. Gao, F. Tao, J. Ren, Unusually low thermal conductivity of atomically thin 2d tellurium, Nanoscale 10 (2018) 12997–13003, https://doi.org/10.1039/c8nr01649f.

[43] Z. Gao, G. Liu, J. Ren, High thermoelectric performance in two-dimensional tellurium: an ab initio study, ACS Appl. Mater. Interfaces 10 (2018) 40702–40709, https://doi.org/10.1021/acsami.8b11836.

[44] C. Lin, W. Cheng, G. Chai, H. Zhang, Thermoelectric properties of two-dimensional selenene and tellurene from group-vi elements, Phys. Chem. Chem. Phys. 20 (2018) 24250–24256, https://doi.org/10.1039/c8cp04069a.

[45] G. Qiu, S. Huang, M. Segovia, P.K. Venuthurumilli, Y. Wang, W. Wu, X. Xu, P.D. Ye, Thermoelectric performance of 2d tellurium with accumulation contacts, Nano Lett. 19 (2019) 1955–1962, https://doi.org/10.1021/acs.nanolett.8b05144.

[46] G. Liu, Z. Gao, J. Ren, Anisotropic thermal expansion and thermodynamic properties of monolayer β-te, Phys. Rev. B 99 (2019), https://doi.org/10.1103/PhysRevB.99.195436.

[47] C.Y. Ho, R.W. Powell, P.E. Liley, Thermal conductivity of the elements, J. Phys. Chem. Ref. Data 1 (1972) 279–421, https://doi.org/10.1063/1.3253100.

[48] X. Wang, B. Huang, Computational study of in-plane phonon transport in si thin films, Sci. Rep. 4 (2014) 6399, https://doi.org/10.1038/srep06399.

[49] J.E. Turney, A.J.H. McGaughey, C.H. Amon, In-plane phonon transport in thin films, J. Appl. Phys. 107 (2010), https://doi.org/10.1063/1.3296394.

[50] A. Kundu, N. Mingo, D.A. Broido, D.A. Stewart, Role of light and heavy embedded nanoparticles on the thermal conductivity of sige alloys, Phys. Rev. B 84 (2011): 125426, https://doi.org/10.1103/PhysRevB.84.125426.

[51] S.-i. Tamura, Isotope scattering of dispersive phonons in ge, Phys. Rev. B 27 (1983) 858–866, https://doi.org/10.1103/PhysRevB.27.858.

[52] W. Li, J. Carrete, N. Mingo, Thermal conductivity and phonon linewidths of monolayer mos2 from first principles, Appl. Phys. Lett. 103 (2013), https://doi.org/10.1063/1.4850995.

[53] T. Feng, L. Lindsay, X. Ruan, Four-phonon scattering significantly reduces intrinsic thermal conductivity of solids, Phys. Rev. B 96 (2017), https://doi.org/10.1103/PhysRevB.96.161201.

[54] W. Li, J. Carrete, N.A. Katcho, N. Mingo, Shengbte: a solver of the Boltzmann transport equation for phonons, Comput. Phys. Commun. 185 (2014) 1747–1758, https://doi.org/10.1016/j.cpc.2014.02.015.

[55] G. Kresse, J. Furthmuller, Efficient iterative schemes for ab initio total-energy calculations using a plane-wave basis set, Phys. Rev. B Condens. Matter 54 (1996) 11169–11186, https://doi.org/10.1103/physrevb.54.11169.

[56] G. Kresse, D. Joubert, From ultrasoft pseudopotentials to the projector augmented-wave method, Phys. Rev. B 59 (1999) 1758–1775, https://doi.org/10.1103/PhysRevB.59.1758.

[57] J.P. Perdew, K. Burke, M. Ernzerhof, Generalized gradient approximation made simple, Phys. Rev. Lett. 77 (1996) 3865–3868, https://doi.org/10.1103/PhysRevLett.77.3865.

[58] H.J. Monkhorst, J.D. Pack, Special points for brillouin-zone integrations, Phys. Rev. B 13 (1976) 5188–5192, https://doi.org/10.1103/PhysRevB.13.5188.

[59] A. Togo, I. Tanaka, First principles phonon calculations in materials science, Scripta Mater. 108 (2015) 1–5, https://doi.org/10.1016/j.scriptamat.2015.07.021.

[60] O. Hellman, I.A. Abrikosov, Temperature-dependent effective third-order interatomic force constants from first principles, Phys. Rev. B 88 (2013), https://doi.org/10.1103/PhysRevB.88.144301.

[61] J.-P.M. Péraud, N.G. Hadjiconstantinou, Efficient simulation of multidimensional phonon transport using energy-based variance-reduced Monte Carlo formulations, Phys. Rev. B 84 (2011), https://doi.org/10.1103/PhysRevB.84.205331.

[62] Q. Hao, G. Chen, M.-S. Jeng, Frequency-dependent Monte Carlo simulations of phonon transport in two-dimensional porous silicon with aligned pores, J. Appl. Phys. 106 (2009): 114321, https://doi.org/10.1063/1.3266169.

[63] M.D. Kamatagi, R.G. Vaidya, N.S. Sankeshwar, B.G. Mulimani, Low-temperature lattice thermal conductivity in free-standing gan thin films, Int. J. Heat Mass Tran. 52 (2009) 2885–2892, https://doi.org/10.1016/j.ijheatmasstransfer.2008.10.032.

[64] D.T. Morelli, J.P. Heremans, G.A. Slack, Estimation of the isotope effect on the lattice thermal conductivity of group iv and group iii-v semiconductors, Phys. Rev. B 66 (2002), https://doi.org/10.1103/PhysRevB.66.195304.

[65] J. Ma, X. Wang, B. Huang, X. Luo, Effects of point defects and dislocations on spectral phonon transport properties of wurtzite gan, J. Appl. Phys. 114 (2013): 074311, https://doi.org/10.1063/1.4817083.

[66] R. Wu, R. Hu, X. Luo, First-principle-based full-dispersion Monte Carlo simulation of the anisotropic phonon transport in the wurtzite gan thin film, J. Appl. Phys. 119 (2016): 145706, https://doi.org/10.1063/1.4945776.

[67] Z.X. Hu, X. Kong, J. Qiao, B. Normand, W. Ji, Interlayer electronic hybridization leads to exceptional thickness-dependent vibrational properties in few-layer black phosphorus, Nanoscale 8 (2016) 2740–2750, https://doi.org/10.1039/c5nr06293d.

[68] X. Wu, Q. Tao, D. Li, Q. Wang, X. Zhang, H. Jin, J. Li, S. Wang, X. Xu, Unprecedently low thermal conductivity of unique tellurium nanoribbons, Nano Res. 14 (2021) 4725–4731, https://doi.org/10.1007/s12274-021-3414-7.

[69] S.N. Shirodkar, U.V. Waghmare, Emergence of ferroelectricity at a metal-semiconductor transition in a $1t$ monolayer of ${\mathrm{mos}}_{2}$, Phys. Rev. Lett. 112 (2014): 157601, https://doi.org/10.1103/PhysRevLett.112.157601.

[70] S. Lee, F. Yang, J. Suh, S. Yang, Y. Lee, G. Li, H. Sung Choe, A. Suslu, Y. Chen, C. Ko, J. Park, K. Liu, J. Li, K. Hippalgaonkar, J.J. Urban, S. Tongay, J. Wu, Anisotropic in-plane thermal conductivity of black phosphorus nanoribbons at temperatures higher than 100 k, Nat. Commun. 6 (2015) 8573, https://doi.org/10.1038/ncomms9573.

[71] Y. Chen, B. Peng, C. Cong, J. Shang, L. Wu, W. Yang, J. Zhou, P. Yu, H. Zhang, Y. Wang, C. Zou, J. Zhang, S. Liu, Q. Xiong, H. Shao, Z. Liu, H. Zhang, W. Huang, T. Yu, In-plane anisotropic thermal conductivity of few-layered transition metal dichalcogenide td-wte2, Adv. Mater. 31 (2019): e1804979, https://doi.org/10.1002/adma.201804979.

[72] L. Chen, W. Zhang, H. Zhang, J. Chen, C. Tan, S. Yin, G. Li, Y. Zhang, P. Gong, L. Li, In-plane anisotropic thermal conductivity of low-symmetry pdse2, Sustainability 13 (2021), https://doi.org/10.3390/su13084155.

[73] X. Li, S. Lee, Crossover of ballistic, hydrodynamic, and diffusive phonon transport in suspended graphene, Phys. Rev. B 99 (2019), https://doi.org/10.1103/PhysRevB.99.085202.

[74] S. Maintz, V.L. Deringer, A.L. Tchougreeff, R. Dronskowski, Lobster: a tool to extract chemical bonding from plane-wave based dft, J. Comput. Chem. 37 (2016) 1030–1035, https://doi.org/10.1002/jcc.24300.